



Motor guidance by long-range communication on the microtubule highway

Sithara S. Wijeratne^{ab,1}, Shane A. Fiorenza^{c1}, Alex E. Neary^b, Radhika Subramanian^{ab,1,2,3}, and Meredith D. Betterton^{c,d,e,1,2,3}

Edited by Stefan Diez, Center for Molecular Bioengineering, Technische Universität Dresden, Dresden, Germany; received November 20, 2021; accepted May 2, 2022 by Editorial Board Member Yale E. Goldman

Coupling of motor proteins within arrays drives muscle contraction, flagellar beating, chromosome segregation, and other biological processes. Current models of motor coupling invoke either direct mechanical linkage or protein crowding, which rely on short-range motor–motor interactions. In contrast, coupling mechanisms that act at longer length scales remain largely unexplored. Here we report that microtubules can physically couple motor movement in the absence of detectable short-range interactions. The human kinesin-4 Kif4A changes the run length and velocity of other motors on the same microtubule in the dilute binding limit, when approximately 10-nm-sized motors are much farther apart than the motor size. This effect does not depend on specific motor–motor interactions because similar changes in Kif4A motility are induced by kinesin-1 motors. A micrometer-scale attractive interaction potential between motors is sufficient to recreate the experimental results in a biophysical model. Unexpectedly, our theory suggests that long-range microtubule-mediated coupling affects not only binding kinetics but also motor mechanochemistry. Therefore, the model predicts that motors can sense and respond to motors bound several micrometers away on a microtubule. Our results are consistent with a paradigm in which long-range motor interactions along the microtubule enable additional forms of collective motor behavior, possibly due to changes in the microtubule lattice.

kinesin | motors | microtubules | cytoskeleton

Diverse cellular processes rely on coordinated activity of cytoskeletal motor proteins. For example, minifilaments made of multiple myosin motors pull actin filaments together to contract muscle (1, 2). Similarly, dynein motors line the microtubule doublet and collectively induce the oscillatory beating of motile flagella (3, 4). Trains of motors mediate intraflagellar transport, which is essential for assembly and maintenance of cilia and flagella (5, 6). Force balance between plus- and minus-end-directed motors that cross-link microtubules contributes to mitotic spindle organization (7–10). Similarly, tug-of-war between opposite polarity motors underlies bidirectional cargo transport (11–13). For all of these processes, the activity of multiple motors is coupled.

Currently, the best-understood mechanisms of motor–motor coupling fall into two categories: protein crowding and mechanical linkage. Motors can be mechanically linked, either by directly binding to each other or by binding to the same cargo. For example, in myosin minifilaments many motors form an ensemble that collectively generates force to contract muscles against high load (14). Alternatively, motors that are densely crowded on cytoskeletal filaments can have altered activity due to short-range steric interactions and/or cooperativity (15, 16). Kinesin-1 motors form clusters due to short-range attractive interactions, for example (17, 18). Kinesins that regulate microtubule dynamic instability typically accumulate at microtubule ends where their motility changes. The activity of the microtubule-destabilizing kinesin-8 Kip3p is altered in dense clusters at the ends of microtubules (19–21). Another prototypical example is the mitotic spindle-associated kinesin-4 protein Kif4A, which forms clusters at microtubule ends (hereafter referred to as “end tags”) and regulates microtubule length (22–24). Short-range interactions are well studied and recognized as important for motor ensemble function. However, whether coupling between proteins at longer length scales contributes to the organization of motor ensembles remains unclear.

Recent work has provided hints of long-range interactions between motors on microtubules. An important early study found that kinesin-1 motors can alter the binding affinity of other kinesin-1 motors micrometers away along microtubules (25). This effect can result in cooperative binding of kinesins to the same microtubule. More recent work has suggested that the surprising long-range interactions may be due to changes in the microtubule lattice due to motor binding (26, 27) that alter binding kinetics (25, 26). Modeling work has proposed that the lattice changes may arise from elastic

Significance

Motor proteins that walk on cytoskeletal filaments and exert force work together for muscle contraction, sperm swimming, and cell division, among other biological processes. Current mechanisms of motor–motor coupling involve them being physically close together along cytoskeletal filaments like microtubules. Here we report that motors on microtubules can physically interact over long distances. The human kinesin-4 Kif4A changes the motion of other motors on the same microtubule, even when they are widely separated. A micrometer-scale interaction between motors in a computational model can explain the results. Our theory suggests that this long-range coupling affects not only binding kinetics but also the way the motor steps. Therefore, motors can sense and respond to motors bound far away.

Author contributions: S.S.W., S.A.F., R.S., and M.D.B. designed research; S.S.W. and S.A.F. performed research; S.S.W., S.A.F., and A.E.N. contributed new reagents/analytic tools; S.S.W., S.A.F., R.S., and M.D.B. analyzed data; and S.S.W., S.A.F., R.S., and M.D.B. wrote the paper.

The authors declare no competing interest.

This article is a PNAS Direct Submission. S.D. is a guest editor invited by the Editorial Board.

Copyright © 2022 the Author(s). Published by PNAS. This article is distributed under Creative Commons Attribution-NonCommercial-NoDerivatives License 4.0 (CC BY-NC-ND).

¹S.S.W. and S.A.F. contributed equally to this work.

²To whom correspondence may be addressed. Email: radhika@molbio.mgh.harvard.edu or mdb@colorado.edu.

³R.S. and M.D.B. contributed equally to this work.

This article contains supporting information online at <https://www.pnas.org/lookup/suppl/doi:10.1073/pnas.2120193119/-DCSupplemental>.

Published July 7, 2022.

anisotropy (28). Further, kinesin-1 motors have been shown to cause lattice defects (29). These results are part of a growing body of evidence that motor and nonmotor microtubule-associated proteins can structurally alter the tubulin lattice. Lattice effects are proposed to influence microtubule dynamics directly or indirectly by altering the activity of regulatory proteins (30, 31). Currently, whether long-distance coupling through the “medium” of the microtubule can affect motile properties of motor proteins is not known. It further remains unclear whether long-range coupling mechanisms can dynamically sense and respond to motor density on microtubules, particularly at low concentration. Finally, whether coupling between proteins at a longer length scale contributes to the formation of motor ensembles/clusters is unknown. Hence, we have a limited understanding of whether concentration-dependent long-range coupling might be a general mechanism that determines the spatial organization of motors on microtubules.

In this work, we report unexpected long-range coupling between Kif4A motors on microtubules at low density. This coupling, which appears to have a range of several micrometers, leads to a density-dependent change in Kif4A processivity and speed at a picomolar motor concentration, where short-range protein–protein interactions are unlikely. The results indicate that kinesins can influence the movement of motor molecules that are widely separated on microtubules, even without detectable physical short-range coupling, oligomerization, external binding partners, or specific tubulin posttranslational modification. Computational modeling suggests that long-range coupling is likely to affect the mechanochemical stepping cycle of the motor in addition to the binding kinetics. At higher protein concentration, motor coupling on the nanometer and the micrometer scale coexists and results in the organization of microtubule-length-dependent Kif4A end tags, which is not predicted for moderately processive motors like Kif4A. These observations enlarge our understanding of how long-range interactions allow communication between motors separated on the micrometer length scale.

Results

The motile kinesin-4 motor protein Kif4A accumulates at microtubule ends, where it binds with high affinity (23, 24). In contrast to other highly processive kinesins or complexes, such as Kip3p (19–21) or the PRC1-Kif4A complex (24), Kif4A alone is only moderately processive, with an average estimated run length of about 1 μm (23). Despite this, previously published data show that Kif4A end tags are sensitive to overall microtubule length for microtubules up to 14 μm long (24). To understand how motors could possibly exhibit length-dependent behavior at length scales an order of magnitude larger than their average run length, we investigated the formation of end tags by Kif4A motors.

To measure end-tag formation and its dependence on microtubule length and motor concentration, we reconstituted the activity of Kif4A on single microtubules. For these studies, we used a total internal reflection fluorescence (TIRF) microscopy assay as reported previously (24, 33). First, rhodamine-labeled, taxol-stabilized microtubules were biotinylated and immobilized on a glass coverslip (Fig. 1A). Next, GFP-tagged Kif4A (0.02 nM) was added to the flow chamber for 5 min and then imaged. Multiwavelength imaging of rhodamine-labeled microtubules and Kif4A-GFP showed that Kif4A preferentially accumulates at the plus end of microtubules, as observed previously (Fig. 1B) (24). With increasing Kif4A concentration (0.02 to 6 nM), the length of the end tags increases. In particular, the micrometer-sized end tags at higher Kif4A concentration (4 nM) resemble those formed

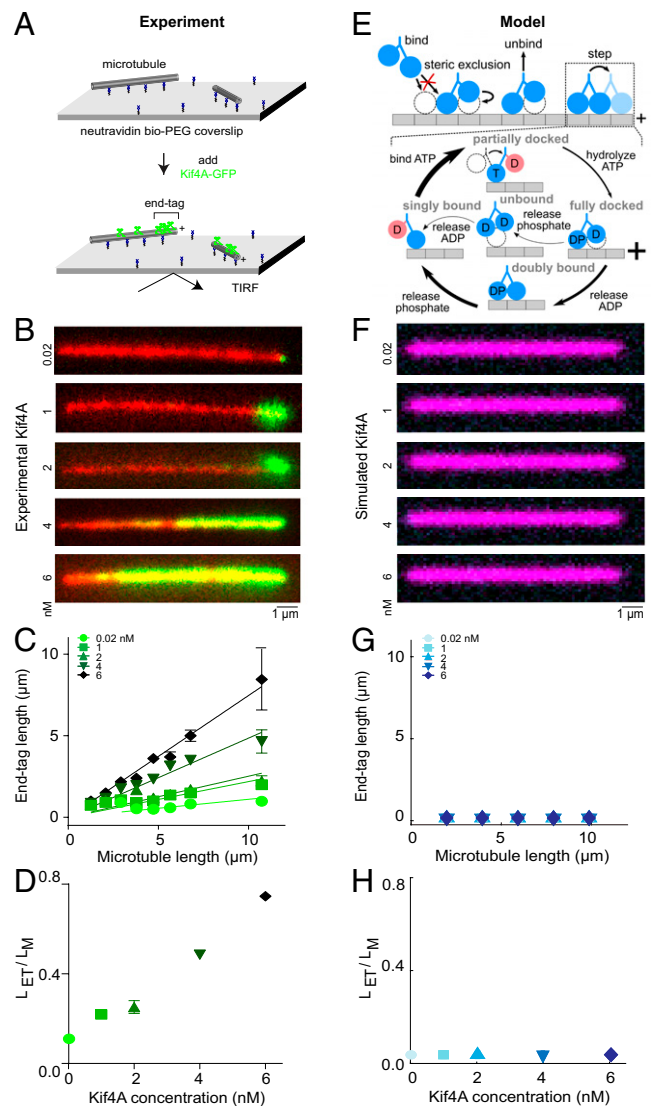


Fig. 1. The kinesin-4 motor Kif4A forms microtubule-length-dependent end tags, but a minimal motor model does not reproduce the experimental observations. (A) Schematic of the in vitro assay used to study Kif4A-GFP (green) on single microtubules (gray). (B) Representative fluorescence micrographs showing end-tag formation with Kif4A-GFP concentration from 0.02 to 6 nM. Images show X-rhodamine-labeled microtubules (red) with Kif4A-GFP (green). (C) End-tag length versus microtubule length in assays with Kif4A-GFP concentration from 0.02 to 6 nM: 0.02 nM (slope 0.11 ± 0.02), 1 nM (slope 0.22 ± 0.02), 2 nM (slope 0.25 ± 0.03), 4 nM (slope 0.49 ± 0.02), and 6 nM (slope 0.75 ± 0.02). (D) Slope (end-tag length divided by microtubule length) versus Kif4A concentration. (E) Model overview. Motors can bind, unbind, and step, constrained by steric interactions. *Inset*, model mechanochemical cycle. See *SI Appendix* and previous work (32). (F) Simulated fluorescence images created from the model using 10- μm -long microtubules and with Kif4A concentration from 0.02 to 6 nM. (G) Simulated end-tag length versus microtubule length. (H) Slope (simulated end-tag length divided by microtubule length) versus Kif4A concentration.

from the collective activity of Kif4A and PRC1 at concentrations of 1.5 and 0.1 to 0.4 nM, respectively (24). We measured the end-tag length and intensity over a range of filament lengths up to 13 μm (Fig. 1C and *SI Appendix*, Fig. S1A). The data fit well to a straight line, where the slope corresponds to the fraction of the microtubule length that is the end tag (Fig. 1D and *SI Appendix*, Fig. S1B). These results show microtubule-length dependence of end tags formed by Kif4A alone.

We then sought to understand how Kif4A motors with a run length of only $\sim 1 \mu\text{m}$ can form length-dependent end tags on microtubules that are $\sim 10 \mu\text{m}$ long by developing a biophysical model of Kif4A motion and accumulation on microtubules

(SI Appendix) (32). The motor model includes binding to and unbinding from microtubules, stepping via a mechanochemical cycle, and steric exclusion. A single protofilament of the microtubule is represented as a one-dimensional lattice, where each 8-nm tubulin dimer is represented by a discrete binding site. This model builds on previous theory of motor accumulation on microtubules and traffic jams (21, 34–40).

To investigate how motor coupling might alter Kif4A behavior, we modeled motor stepping with a mechanochemical cycle driven by ATP hydrolysis, building on previous work (41–47). We constructed the model based on the kinesin-1 stepping cycle (Fig. 1E) (48–54). While the details of the mechanochemical cycle may be different for Kif4A compared to kinesin-1, our model predictions are similar for any model that includes cyclic asynchronous binding and unbinding of two binding heads (50, 55). In our model, the nucleotide hydrolysis rate determines motor velocity, while the relative rates of second-head binding and first-head unbinding determine processivity (SI Appendix) (32).

To model motor-dense end tags, we implemented steric interactions. In the model no binding site can be occupied by more than one motor head. If a motor is blocked from stepping forward by another motor in front of it, the rear head can still unbind, causing the motor to become stuck in the singly bound state. We constrained parameters of the model using motor processivity and velocity from previously published data on Xklp1 (23), and the motor on rate was estimated from experiments imaging the binding to and motility of Kif4A-GFP on microtubules at low motor density (24).

In our simulations of this model, end tags do not form and motor accumulation does not vary with microtubule length (Fig. 1F–H). A simple analytic model of end-tag formation shows the same result (SI Appendix, SI Text and Fig. S2), consistent with our intuition that a motor with a run length of only 1.2 μm cannot show enhanced accumulation on microtubules several micrometers long.

The lack of end-tag formation in the model suggests that the model is missing key mechanisms, such as interactions between motors that alter their behavior in dense ensembles. We therefore examined whether cooperative interactions between motors might be required for end tags. Previous work on kinesin-1 found that the motors cluster together on microtubules more than would be expected for purely noninteracting motors (17, 18). These data were consistent with a short-range (nearest-neighbor) attractive interaction between motors with an estimated energy of 1.6 to 1.8 $k_B T$ (17, 18). A similar short-range interaction would be expected if Kif4A can physically interact with nearby motors, perhaps by binding between C-terminal tail domains, which typically mediate the interactions of kinesins with protein cargo. To test whether such a short-range interaction could explain end-tag formation, we implemented a nearest-neighbor interaction that lowers the unbinding rate of adjacent motors (SI Appendix) (32). Nearest-neighbor interactions between Kif4A motors in the model cannot fully explain end-tag formation, even if the interaction energy is increased to 10 $k_B T$ (SI Appendix, Fig. S3A).

Another missing mechanism could be higher motor processivity, for example if previous measurements underestimated the run length of Kif4A. Therefore, we modeled the effects of increasing processivity by up to a factor of 10, to 12 μm . (Note that this test was done without nearest-neighbor interactions.) Even with this high processivity, end tags did not form (SI Appendix, Fig. S3B). This is because in the crowded end tag, most motors in the model have one head bound, which is a weak binding state (52) that controls their lifetime in the end tag. We identified only one mechanism that can partially succeed in reproducing end tags: In

our simplified analytic model, if we reduce the overall unbinding rate of motors within the end tag by a factor of 20, a type of end tag can form (SI Appendix, Fig. S2C). This simplified model favors end-tag formation by assuming that all motors are reaching the end tag (SI Appendix). The model's failure to reproduce end tags without a drastically reduced off rate shows that a steady-state accumulation model cannot explain end-tag formation. Even with the low unbinding rate of motors from the ends, this model does not reproduce experiments: The variation of end-tag length with bulk motor concentration is sublinear (SI Appendix, Fig. S2D). These results suggest that another, unknown mechanism may be required to explain how Kif4A can form end tags.

To investigate coupling between Kif4A motors bound to microtubules, we examined the behavior of single Kif4A-GFP molecules on microtubules with varying concentration of unlabeled Kif4A (Fig. 2). Photobleaching experiments and initial fluorescence intensity analysis of Kif4A-GFP molecules in our preparation show that the protein is largely dimeric (SI Appendix, Fig. S4A). At 20 pM, single Kif4A-GFP molecules moved only short distances before dissociation (Fig. 2A). However, the addition of picomolar amounts of unlabeled Kif4A (30 to 400 pM) led to longer unidirectional movements of individual Kif4A-GFP molecules. For example, when just 60 pM of unlabeled Kif4A was added, the average run length and lifetime of Kif4A increased by a factor of ~ 2 and ~ 4 , respectively (Fig. 2B, C, E, and F), along with a twofold reduction in the average velocity, as determined by analysis of individual motile tracks from kymographs (Fig. 2D and G and SI Appendix, SI Methods). Tracks that exhibited pausing (defined as nonmovement for at least 2 s or five time frames) or terminated at end tags were not included in the quantitative analysis. These data suggest that even at subnanomolar protein concentration where motors are widely separated, the processivity and velocity of the motor are sensitive to small changes in protein density on microtubules.

To avoid potential bias in measurement of motility parameters from kymographs, we next used an independent particle-tracking method to analyze the data (SI Appendix, SI Methods). Events with fluorescence intensity above a threshold and those terminating at end tags were excluded (SI Appendix, Fig. S5). Since some of the tracks showed a mixture of movement and pausing, we separately classified and examined tracks that move continuously and those that exhibit pauses (any event greater than three time frames where the instantaneous velocity of two points on the track is less than 5 nm/s). We find that the events with pauses are a minor population and excluding them does not alter the results (SI Appendix, Figs. S6–S15). Furthermore, the average pause duration of motors does not significantly change with motor concentration (SI Appendix, Fig. S16). We then performed a series of correlation analyses that confirm that the changes in velocity and lifetime do not arise due to events with long pauses or due to higher-intensity Kif4A-GFP molecules that may be aggregated (SI Appendix, Fig. S17). The intensity distribution of Kif4A-GFP molecules remained approximately constant as Kif4A concentration was increased, consistent with the idea that large protein aggregates do not underlie the changes in Kif4A-GFP motility with increasing motor concentration (SI Appendix, Fig. S18). Together, these experimental observations and analysis point to a mechanism whereby Kif4A molecules can alter the behavior of other distant Kif4A motors on a microtubule.

If the hypothesized long-range motor coupling is mediated via the microtubule, it might also occur with change in density of other kinesins besides Kif4A. To test this, we measured the motility of single Kif4A-GFP molecules in the presence of increasing concentration (30 to 400 pM) of unlabeled *Drosophila*

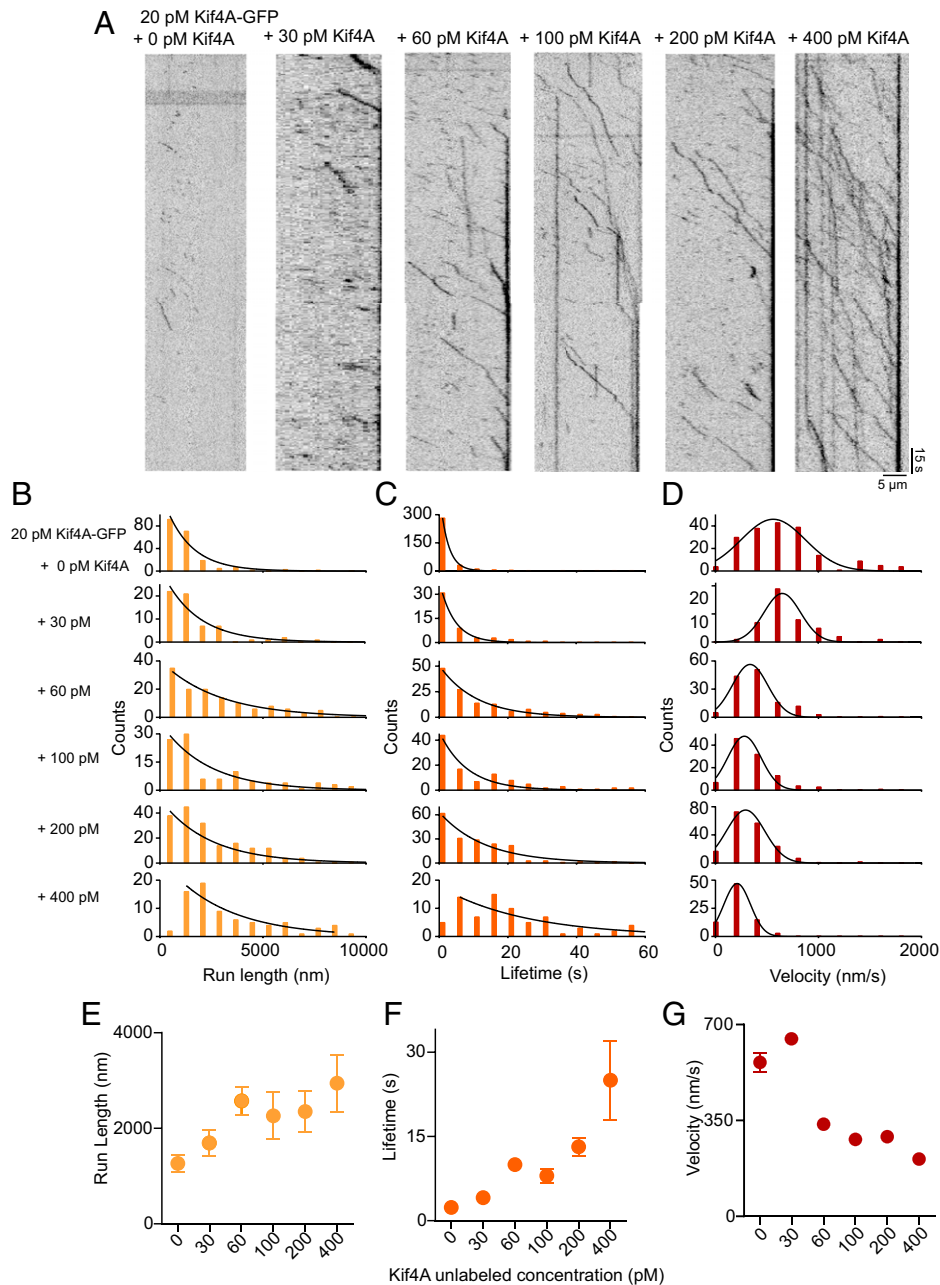


Fig. 2. Single-molecule analysis of Kif4A-GFP movement in the presence of Kif4A-unlabeled. (A) Kymographs obtained from time-lapse image sequence acquired in examining microtubule interaction of Kif4A-GFP (20 pM) in presence of 0, 30, 60, 100, 200, and 400 pM Kif4A-unlabeled. Kymographs are aligned so that the plus ends of microtubules appear on the right. (B–D) Histograms of the run length (B), lifetime (C), and average velocity (D) obtained from time-lapse image sequence acquired in examining microtubule interaction of Kif4A-GFP (20 pM) in presence of 0, 30, 60, 100, 200, and 400 pM Kif4A-unlabeled. The run length and lifetime histograms were fitted to an exponential function. The average velocity histogram was fitted to a Gaussian distribution. (E) Average run length versus Kif4A concentration, obtained from the exponential fits in C: 0 pM (1,265 nm, $n = 205$), 30 pM (1,700 nm, $n = 62$), 60 pM (2,572 nm, $n = 134$), 100 pM (2,262 nm, $n = 106$), 200 pM (2,350 nm, $n = 182$), and 400 pM (2,946 nm, $n = 78$). (F) Average lifetime versus Kif4A concentration, obtained from the exponential fits in D: 0 pM (2.4 s, $n = 205$), 30 pM (4.3 s, $n = 50$), 60 pM (10 s, $n = 134$), 100 pM (8 s, $n = 106$), 200 pM (13.6 s, $n = 182$), and 400 pM (25 s, $n = 78$). (G) Average velocity versus Kif4A concentration, obtained from the Gaussian fits in E: 0 pM (562 nm/s, $n = 205$), 30 pM (675 nm/s, $n = 43$), 60 pM (336 nm/s, $n = 134$), 100 pM (281 nm/s, $n = 106$), 200 pM (291 nm/s, $n = 182$), and 400 pM (209 nm/s, $n = 78$). The error bars represent the SEM.

melanogaster kinesin-1 dimers (amino acids 1 to 401; referred to as K401). K401 is a minimal kinesin-1 dimer comprising the motor domain, the neck linker, and the first dimerization coiled-coil domain. When the total motor concentration was increased by adding unlabeled K401, single Kif4A-GFP molecules moved more processively and exhibited long unidirectional runs (Fig. 3). With 60 pM of unlabeled K401 in an assay with 20 pM Kif4A-GFP, the average run length and lifetime increased by a factor of ~ 2 and ~ 4 , respectively, while the average velocity decreased. These results show Kif4A processivity and velocity are sensitive to

the density of a motor of a different kinesin family. Because K401 lacks the C-terminal cargo-binding domains typically responsible for protein–protein interactions in kinesins, these data support the idea that the motor-coupling interactions that impact Kif4A motility likely do not arise from short-range protein–protein interactions. Further supporting the idea that oligomerization is unlikely to explain our results, significant intensity increase of Kif4A-GFP molecule spots was not detected in these experiments, and biochemical binding assays do not detect any interaction between Kif4A and K401 in solution (*SI Appendix, Fig. S19*).

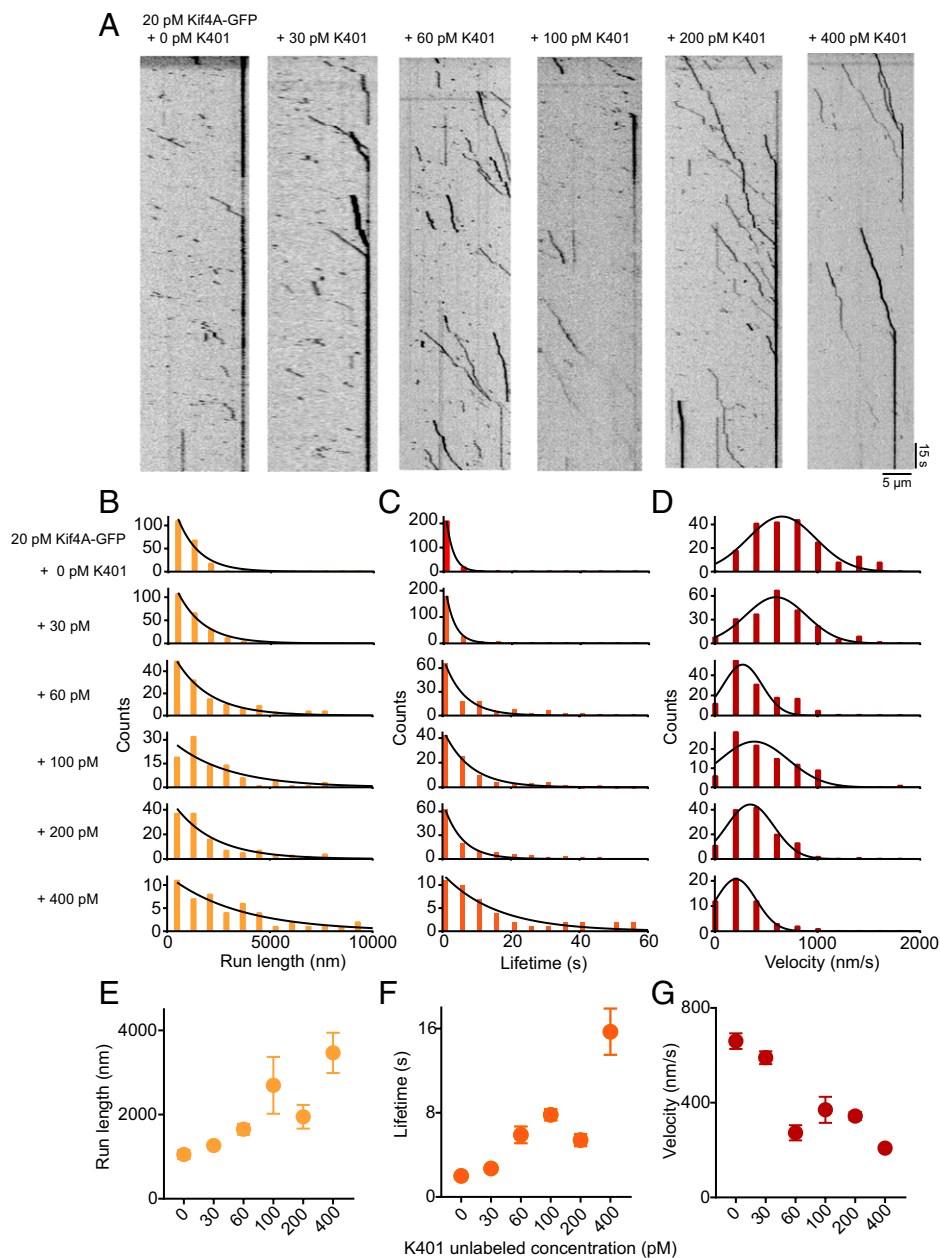


Fig. 3. Single-molecule analysis of Kif4A-GFP movement in the presence of K401-unlabeled. (A) Kymographs obtained from time-lapse image sequence of microtubules with Kif4A-GFP (20 pM) in presence of 0, 30, 60, 100, 200, and 400 pM K401-unlabeled. Kymographs are aligned so that the plus ends of microtubules appear on the right. (B–D) Histograms of the run length (B), lifetime (C), and average velocity (D) obtained from time-lapse image sequence of Kif4A-GFP (20 pM) in presence of 0, 30, 60, 100, 200, and 400 pM K401-unlabeled. Run length and lifetime histograms were fitted to an exponential function. The average velocity histogram was fitted to a Gaussian distribution. (E) Average run length versus K401 concentration, obtained from the exponential fit in B: 0 pM (1,050 nm, $n = 202$), 30 pM (1,264 nm, $n = 228$), 60 pM (1,650 nm, $n = 140$), 100 pM (2,694 nm, $n = 96$), 200 pM (1,949 nm, $n = 129$), and 400 pM (3,465 nm, $n = 51$). (F) Average lifetime versus K401 concentration, obtained from the exponential fit in C: 0 pM (1.5 s, $n = 202$), 30 pM (2.7 s, $n = 228$), 60 pM (5.9 s, $n = 140$), 100 pM (7.8 s, $n = 96$), 200 pM (5.4 s, $n = 129$), and 400 pM (15.7 s, $n = 51$). (G) Average velocity versus K401 concentration, obtained from the Gaussian fits in D: 0 pM (660 nm/s, $n = 202$), 30 pM (590 nm/s, $n = 228$), 60 pM (273 nm/s, $n = 140$), 100 pM (370 nm/s, $n = 96$), 200 pM (343 nm/s, $n = 129$), and 400 pM (208, $n = 51$). The error bars represent the SEM.

Together, our experimental results with varying Kif4A and K401 density suggest that motility of single Kif4A motors is modulated by coupling of motors widely separated along the microtubule.

To facilitate measurement of single motors, the experiments above used Kif4A-GFP with mixtures of fluorescent and non-fluorescent proteins. Based on motor density in experiments performed at 20 pM Kif4A, we predict that individual motors are minimally separated by hundreds of nanometers (several camera pixels) in the picomolar motor concentration range. However, clustering or aggregation of unlabeled motors cannot be directly observed optically and could hypothetically affect our results.

To test whether the increase in lifetime and reduction in velocity at low density might result from motor clustering, we performed two-color imaging in experiments where both populations of motors were fluorescently labeled (Fig. 4). We purified recombinant Kif4A-mCherry (all labeled) and dimeric K401-clip labeled with Alexa-647. Two independent K401 preparations resulted in labeling efficiencies of 15% monomer (15 to 28% dimer) and 58% monomer (58 to 82% dimer; *SI Appendix, SI Methods*). Photobleaching experiments and intensity analysis are consistent with these fluorescent proteins being largely dimeric (*SI Appendix, Fig. S4 B–D*). Two-color experiments were

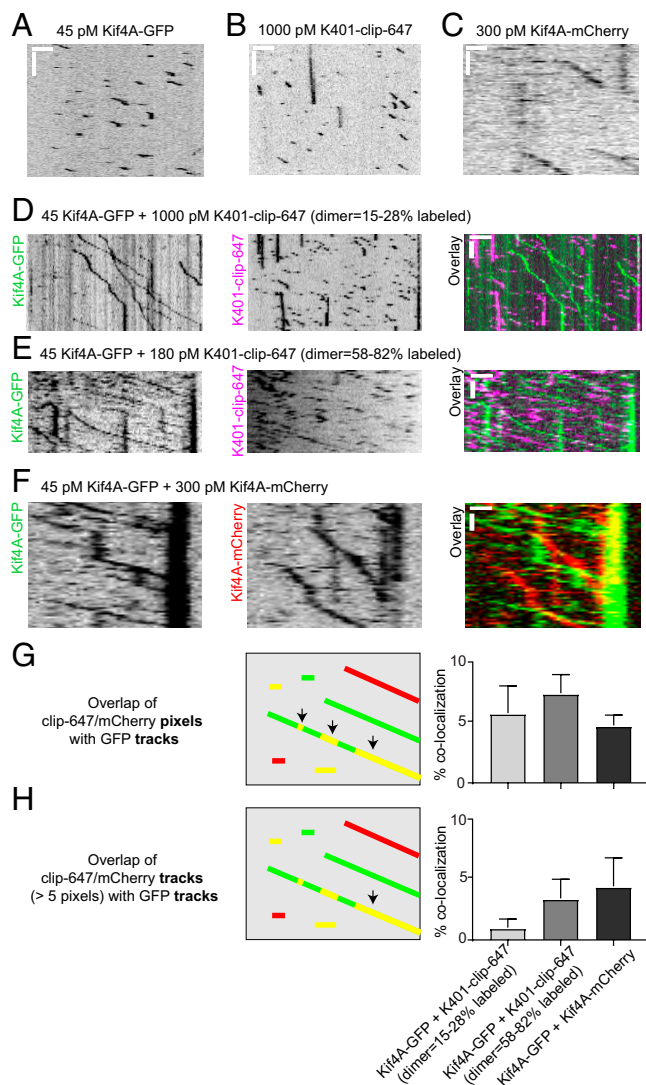


Fig. 4. Single-molecule analysis of Kif4A-GFP movement in the presence of K401-clip-647 or Kif4A-mCherry. (A–F) Kymographs obtained from time-lapse image sequence acquired in examining microtubule interaction of (A) 45 pM Kif4A-GFP (scale bar: $x = 2 \mu\text{m}$; $y = 6 \text{s}$), (B) 1,000 pM K401-clip-647 (scale bar: $x = 5 \mu\text{m}$; $y = 11 \text{s}$), (C) 300 pM Kif4A-mCherry (scale bar: $x = 2 \mu\text{m}$; $y = 7 \text{s}$), (D) 45 pM Kif4A-GFP + 1,000 pM K401-clip-647 (dimer 15 to 28% labeled) (scale bar: $x = 3 \mu\text{m}$; $y = 10 \text{s}$), (E) 45 pM Kif4A-GFP + 180 pM K401-clip-647 (dimer 58 to 82% labeled) (scale bar: $x = 1.5 \mu\text{m}$; $y = 10 \text{s}$), and (F) 45 pM Kif4A-GFP + 300 pM Kif4A-mCherry (scale bar: $x = 1 \mu\text{m}$; $y = 2 \text{s}$). (G and H) Two methods of quantitative analysis of the colocalization of the GFP with either K401-clip-647 or Kif4A-mCherry from the two color experiments from D–F (Materials and Methods). The kymograph schematic and bar graph show percentage of colocalization of (G) clip-647/mCherry pixels with GFP tracks (Kif4A-GFP + K401-clip-647 [dimer = 15 to 28% labeled], mean $6 \pm 2\%$, $n = 11$; Kif4A-GFP + K401-clip-647 [dimer = 58 to 82% labeled], $7 \pm 2\%$, $n = 32$; Kif4A-GFP + Kif4A-mCherry, $5 \pm 1\%$, $n = 50$) and (H) clip-647/mCherry tracks (greater than 5 pixels) with GFP tracks (Kif4A-GFP + K401-clip-647 [dimer = 15 to 28% labeled], mean $1 \pm 1\%$, $n = 24$; Kif4A-GFP + K401-clip-647 [dimer = 58 to 82% labeled], $3 \pm 2\%$, $n = 20$; Kif4A-GFP + Kif4A-mCherry, $5 \pm 2\%$, $n = 51$). The kymograph overlay schematic shows GFP (green lines), clip-647/mCherry (red lines), and the overlap between GFP and clip-647/mCherry (yellow lines). The measured events are indicated by the black arrows. The error is the SEM.

performed with mixtures of Kif4A-GFP and Kif4A-mCherry or Kif4A-GFP and K401-clip-647. To measure colocalization, the experimental conditions were empirically optimized such that sufficient events of both fluorescent motors were observed. We note that quantitative differences in some aspects of motor behavior such as motor processivity between Figs. 4 and 2 likely arise due to differences in protein concentration estimates and activity in different protein preparations.

Visual and kymograph analyses of the experiments with Kif4A-GFP and Kif4A-mCherry show that both the Kif4A populations exhibit longer tracks of movement when the total protein concentration is increased (Fig. 4 A, C, and F). These kymographs rarely show colocalization between the GFP and mCherry signal for a significant time. To quantify this, we measured the fraction of events with colocalized, comoving motors. First, for each Kif4A-GFP track we quantified whether Kif4A-mCherry fluorescence is present for any pixel along the track. Only $\sim 5\%$ of tracks show any level of fluorescence overlap between the two motor populations (Fig. 4G). Second, we applied a more stringent criterion, defining a comoving track as one where continuous colocalization of GFP and mCherry fluorescence is observed for at least five timepoints. This analysis similarly finds that comoving tracks are a small fraction of the total (Fig. 4H).

To look for evidence of transient Kif4A and K401 association, we performed similar two-color experiments with Kif4A-GFP and K401-clip-647. Consistent with previous results, 45 pM of Kif4A-GFP exhibits short processive runs before dissociation (Fig. 4A). The addition of 1,000 pM K401-clip-647 (15 to 28% labeled dimer) or 180 pM K401-clip-647 (58 to 82% labeled dimer) results in much longer runs by Kif4A-GFP (Fig. 4 D and E). Importantly, changes in K401-clip-647 motility with concentration were not apparent (Fig. 4 B, D, and E). Visual and kymograph analysis shows independent tracks corresponding to GFP and Alexa-647 signals. Quantitative colocalization analysis shows that fewer than 10% of Kif4A-GFP have any signal from the clip-647 channel (Fig. 4 G and H).

Together, these results suggest that protein clustering or collisions due to interactions while bound to the microtubule are rare, making it unlikely that the changes in motor activity described here arise from motor colocalization. In addition, we find that the motility of K401 does not change with increasing concentration, while the motility of Kif4A does, consistent with our other measurements (SI Appendix, Fig. S20). Therefore, it appears that Kif4A motors can be coupled even when they are separated by distances orders of magnitude larger than the distance between adjacent tubulin dimers in a microtubule.

To understand possible effects of long-range coupling, we developed a biophysical model with varying hypotheses for motor interactions and compared to the low-density data (Fig. 5) (32). First, we confirmed that a model with only short-range (nearest-neighbor) interactions could not explain our data (Fig. 5 A–D, and M), even with the interaction strength increased up to $10 k_B T$ (SI Appendix, Fig. S21). We then considered what form of long-range interaction might explain the changes in motility we measured. Long-range coupling has been observed previously for kinesin-1, where enhanced binding was observed over $6 \mu\text{m}$ away from a single bound motor (25). This effect appeared additive, resulting in a cascade of motor binding once a sufficient number of motors bind. Based on this, we introduced a long-range potential between motors that is additive up to a maximum saturation energy (SI Appendix) (32). The interaction alters motor binding and unbinding rates, which vary spatially as a Gaussian function. Our coupling model therefore has four parameters: the Gaussian amplitude and width, the saturation energy, and the strength of the nearest-neighbor interaction.

We first considered a model motivated by prior work on kinesin-1 (25), in which the long-range interaction increases the binding rate and decreases the unbinding rate of other motors (Fig. 5 E–H, and N). We note that this effect was included in addition to short-range nearest-neighbor interaction discussed above. After fitting, we found that the long-range interaction allowed our model to qualitatively reproduce changes in motor motility

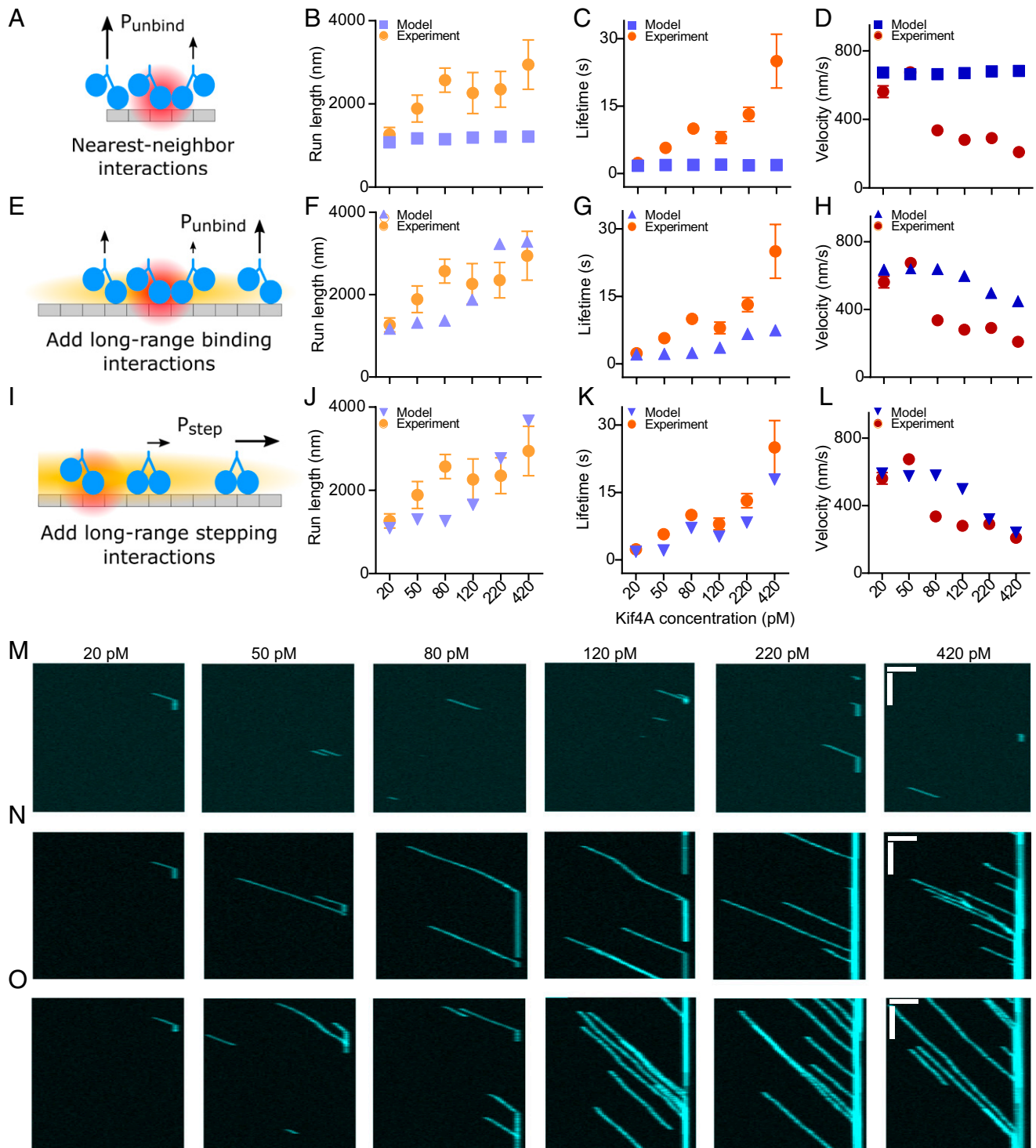


Fig. 5. A model with long-range interactions that affect both motor binding and stepping best reproduces the experimental results. (A) Schematic of nearest-neighbor interaction. The red cloud shows the range of the interaction (one site), and the length of arrows shows relative event probability. In the model, nearest-neighbor interactions decrease the motor unbinding rate but do not affect binding. (B–D) Motor run length, lifetime, and velocity versus motor concentration for simulation (blue) and experiment (orange, red). The strength of the interaction is $2 k_B T$, but the simulation results are similar for interaction strength up to $10 k_B T$ (SI Appendix, Fig. S21). (E) Schematic of long-range binding interaction. The orange cloud represents the range of the interaction (not to scale; the range in simulation is $\sim 1,000$ binding sites). This long-range interaction affects motor binding and unbinding and is implemented in addition to the nearest-neighbor interaction. (F–H) Motor run length, lifetime, and velocity versus motor concentration for simulation (blue) and experiment (orange, red). (I) Schematic of long-range stepping interaction. This long-range interaction acts to reduce overall motor velocity and is implemented in addition to both the long-range binding and nearest-neighbor interactions. (J–L) Motor run length, lifetime, and velocity versus motor concentration for simulation (blue) and experiment (orange, red). (M–O) Simulated kymographs with varying motor concentration and 20-pM visible motors for the model with (M) nearest-neighbor interactions only; (N) nearest-neighbor and long-range binding interactions; and (O) nearest-neighbor, long-range binding, and long-range stepping interactions. The plus ends of microtubules appear on the right. (Horizontal and vertical scale bars: $2 \mu\text{m}$ and 10s , respectively.)

at low density (Fig. 5 E–H, and N). However, the best-fit model did not show strong quantitative agreement with the data, suggesting that long-range interactions that alter motor–microtubule

binding kinetics only partially explain our results. Therefore, we considered whether additional mechanisms might improve the model.

The data show that Kif4A speed slows by a factor of 2 to 3 as motor density is increased. This is surprising given the relatively large separation between motors on the microtubule: In our experiments, dense traffic jams where steric effects could slow motor stepping appeared to be rare. This suggests the possibility that a long-range interaction between motors might alter motor mechanochemistry. To be consistent with our data, the long-range interaction would be predicted to slow motor stepping, which could occur by multiple mechanisms. We chose one plausible candidate: The long-range interaction might slow trailing head detachment such that the stepping velocity decreases (*SI Appendix*) (32, 52). This extension of the model with best-fit parameters agrees well with our experimental data (Fig. 5 *I–L*, and *O*). We note that other mechanisms that slow motor stepping could lead to similar model predictions, so we can make no conclusions about the exact mechanism. However, the model results show that long-range coupling between motors that affects both binding kinetics and stepping can explain changes in Kif4A motility with density.

Comparison of the low-density experimental results to our model suggests that a combination of nearest-neighbor and long-range interactions can explain the increase in Kif4A processivity and decrease in velocity as motor density increases on microtubules. We next asked whether these interactions are sufficient to explain the formation of end tags on microtubules at high density. To test this, we increased the Kif4A concentration in the model while maintaining all other parameters determined by fitting the low-density data. Remarkably, the model predicts end tags that quantitatively match those found experimentally (Fig. 6). In both experiments (Fig. 1*B*) and simulations (Fig. 6 *A* and *B*) at high motor concentrations, we observe the density change at the end tag is abrupt and changes in density along the rest of the lattice are modest. Consistently, lifetime and velocity distributions of molecules near (but not within) and distant from the end tag are similar (*SI Appendix*, Fig. S22). Predicted end-tag length increases both with microtubule length and with motor concentration, as measured (Fig. 6 *A*, *B*, *D*, and *E*).

Fitting of our model to the data estimated a long range of 8 μm (1,000 tubulin dimers). To examine whether a shorter-range model might also suffice, we repeated the fit with the interaction range fixed at lower values of 10 sites (80 nm) and 100 sites (800 nm; *SI Appendix*, Fig. S23 *A* and *C*). With a range of 10 or 100 sites and a larger interaction strength, the model can partially replicate Kif4A motility changes with density. However, in this version of the model the occupancy of motors on the microtubule becomes so high that motor processivity decreases. Consistent with this, when we study the 10- or 100-site-range model at nanomolar motor concentration, microtubules become completely saturated with bound motors. This prevents end-tag formation (*SI Appendix*, Fig. S23 *E* and *G*). If we remove nearest-neighbor interactions and repeat the fitting process, the model shows the same saturation behavior (*SI Appendix*, Fig. S23 *B*, *D*, *F* and *H*). These results suggest that a long-range ($\sim 8 \mu\text{m}$) interaction is required for the model to describe the experiments. Only in the long-range model did we obtain both experimentally observed motility changes at low density and end-tag formation at higher density.

To further dissect which interactions in the model are most important for end-tag formation, we turned off parts of the model individually (Fig. 6*C*). Removing individual cooperative interactions from the model (corresponding to turning off nearest-neighbor interactions, long-range interactions that affect binding, or long-range interactions that affect stepping) decreases predicted end-tag formation. This suggests that the combination of both

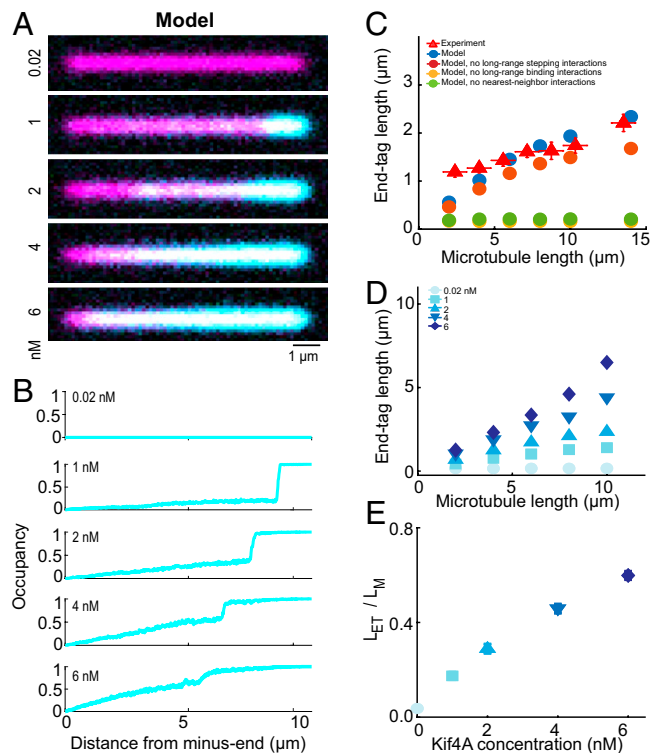


Fig. 6. The computational model with long-range cooperativity that fits low-density experiments predicts length-dependent end tags and Kif4A motility changes with no free parameters. (*A* and *B*) Simulated fluorescence images (*A*) and fractional occupancy profiles (*B*) created from simulations using 10- μm microtubules with varying Kif4A concentration. (*C*) End-tag length versus microtubule length for varying models in simulation (circles) and experiment from ref. 24 (triangles). Blue circles correspond to the final model that includes nearest-neighbor, long-range binding, and long-range stepping interactions. The other red, orange, and green circles show results of the model with one interaction removed. (*D*) Simulated end-tag length versus microtubule length for varying Kif4A concentration. (*E*) Simulated end-tag length divided by microtubule length versus Kif4A concentration. For plots *C–E*, the data points represent the average of different values from four independent simulations. The error bars represent SEM.

long- and short-range motor coupling that we identified in the low-density model together allow Kif4A to form end tags. In the model, the long-range interaction helps increase processivity so that motors reach the end of the microtubule and join the end tag, while the nearest-neighbor interaction slows unbinding to maintain motors in the end tag.

Based on our model results, we propose that long-range motor coupling between Kif4A molecules that increases processivity and lowers velocity contributes to the formation of dense end tags on microtubules. The model predicts that near and in the end tag, the bound lifetime of Kif4A increases and its speed drops. To examine whether these changes occur in end tags, we directly visualized processive movement of single Kif4A molecules at high protein concentration by spiking in Kif4A-GFP (1 nM) with Kif4A-Alexa-647 (7 nM) while observing end-tag formation in real time (Fig. 7*A*). In these experiments, end-tag formation initiates at the microtubule plus end and grows toward the minus end until a steady-state end-tag length is established. Outside the end tag, motors move processively with long plus-end-directed runs ($\gtrsim 5 \mu\text{m}$). Motor velocity in the untagged region of the microtubule was 110 nm/s, but upon encountering the high-density end tag, Kif4A-GFP slowed to 25 nm/s. These results suggest that, consistent with our model predictions, end-tag formation occurs through an increase in Kif4A processivity at high concentration along with a reduction in velocity and dissociation in the end tags.

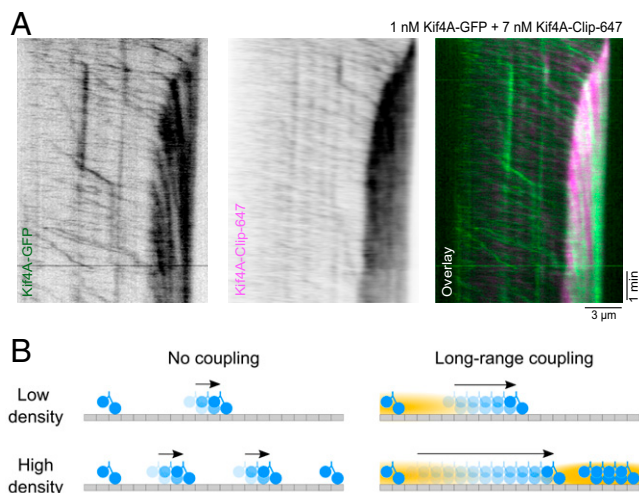


Fig. 7. Illustration of effects of long-range motor coupling. (A) Kymographs obtained from time-lapse sequence acquired in spiking experiments of Kif4A-Clip-647 (7 nM) in presence of Kif4A-GFP (1 nM) on a single microtubule. (B) Schematic shows motors (blue) moving on microtubule (gray) with interaction regions (orange cloud, not to scale). Length of arrows represents motor run length (not to scale). (Top Left) Noninteracting motors do not affect the run length or velocity of other motors. (Top Right) Long-range interactions mean that Kif4A changes the run length and velocity of widely separated motors on the same microtubule. Our theory suggests that this long-range coupling affects not only binding kinetics, but also motor mechanochemistry. (Bottom Left) Noninteracting motors do not change their motility or collective behavior at higher density. (Bottom Right) Long-range coupling promotes the formation of Kif4A end tags at high density. The microtubule therefore responds dynamically to motor binding and alters the behavior of other motors, allowing new forms of collective motor behavior.

Discussion

Here we describe motor communication that spans micrometers without physically linked assembly of motors. We discovered these interactions for Kif4A, a kinesin-4 motor known to cluster at microtubule ends, but the changes in Kif4A motility can also be induced by kinesin-1. Our findings suggest that long-range coupling of motors can impact both the binding and mechanochemistry of motor proteins at low density. This coupling can set up a positive feedback loop whereby motors adaptively increase their processivity, even at picomolar concentration where motors are typically far apart (≥ 200 nm) compared to the motor size (~ 10 nm).

We propose that long-range coupling between motors explains motor-density-dependent changes in processivity and velocity at picomolar motor concentration. Importantly, four alternate mechanisms could not fully explain the low-density motility changes. First, we considered whether an increase in Kif4A processivity could occur through transient clustering. Kif4A clustering is unlikely at the low motor concentration we used, where the motor is a dimer. In the single-molecule experiments, motors are typically separated by at least a few hundred nanometers (several camera pixels). If transient protein-protein interactions occurred that lasted a shorter time than our imaging timescale, such interactions would not be directly visible in our experiments. However, if transient interactions did occur, they would most likely occur between the coiled-coil C-terminal tail domains of the motors. We found that low-density changes in Kif4A motility were also induced by K401, which lacks the C terminus. This argues against a clustering mechanism to explain our results. Further, in multiwavelength imaging of fully labeled Kif4A and K401, colocalization of the two proteins occurred rarely and transiently. Together, these results suggest that clustering is not the mechanism of motility changes at low density.

A second alternative mechanism is collisions between motors that alter their motility, as has been observed previously (15, 16). The low motor concentration in our experiments means that motors are typically widely separated, making collisions rare. The two-color imaging did not reveal significant colocalization, which verifies that the motors remain separated while bound to the microtubule. In addition to these experimental observations, a computational model with short-range (nearest-neighbor) interactions cannot explain our low-density data. In the model, short-range interactions alone are insufficient because the motors are rarely close enough together for collisions or nearest-neighbor interactions to alter their behavior (Movie S1). At high density, motors in our model do indeed collide and this slows their movement, but the long-range interaction occurs separately from this. Therefore, direct steric interactions between motors appear inadequate to explain our results.

A third alternative explanation could be the formation of defects on microtubules by the motors that alter motor stepping (29). Because our experiments do not contain free tubulin dimers, any motor-induced defects in the microtubule lattice would accumulate over time. Therefore, if this mechanism were dominant, we would predict time-dependent changes in Kif4A motility as defects increase. For example, one possibility is that motor processivity would decrease and pausing would increase over time. In contrast to this prediction, we measured consistent Kif4A behavior over time. Therefore, while kinesin-induced defect formation could occur in our experiments, this mechanism appears unlikely to fully explain the findings reported here.

A fourth alternative mechanism is one where kinesin-microtubule interactions result in localized conformational changes in the microtubule lattice, such that motors that subsequently move through the region of altered conformation have altered stepping. This “walking-through-fire” mechanism may be considered a generalization of the idea of defects to include nonpermanent changes to the microtubule. Since Kif4A motors can move ~ 500 nm/s, over 10 s a motor can move 5 μ m, which is a sufficient distance that it could interact with a localized temporary deformation induced by another motor. Therefore, this mechanism could in principle lead to changes in motility of Kif4A. This mechanism would require long-time motility changes of a motor that encounters the “fire pit.” This would result in abrupt changes in motility that would be visible in the kymographs, in contrast to our observations. Further, a single bound motor can alter binding of kinesin-1, as shown previously (25). The walking-through-fire mechanism would not be predicted to affect binding of motors distant from the localized conformational change. Additionally, Muto et al. (25) observed altered binding ahead of the motor (toward the microtubule plus end), which means that a walking motor would not encounter the localized region of conformational change. Therefore, the walking-through-fire mechanism does not appear sufficient to explain both our work and previous work (25).

Because these alternative mechanisms appear insufficient to explain our results, we favor the interpretation that long-range interactions between motors occur. Our minimal experimental system has only two protein components: motors and microtubules. Since we were unable to find definitive evidence of direct motor-motor interactions, changes in the microtubule appear to be the most plausible mechanism to couple distantly separated motors. While our results do not address the structural basis of such a long-range coupling, a natural candidate is motor-induced changes to the microtubule lattice (26, 27), which have previously been shown to induce interactions between motors

at low density that are separated by micrometers (25, 26). In our simulations, the long-range interaction between motors can explain both low-density motility changes and end-tag formation at higher density. Crucially, our computational model assumes that the motor interactions—and, by implication, any changes to the microtubule structure—occur rapidly upon motor binding and reverse rapidly after motor unbinding. This is consistent with previous work that found microtubule lattice changes induced by saturating motor binding are reversible on timescales of seconds to minutes (26, 27). Together, these results suggest that transient, reversible changes to the microtubule lattice can couple motors over micrometers. These results expand the way we think about microtubules as a medium for allosteric coupling between motor proteins.

Previous work on long-range interactions between kinesin-1 motors proposed that the coupling affects motor binding kinetics (25, 26). In our work, the changes to motor velocity with density (at low overall motor concentration) cannot be fully explained by an interaction that affects only the binding kinetics of the motor–microtubule interaction. Therefore, our model results suggest that the long-range cooperativity directly affects motor mechanochemistry.

Our results further differ from previous data on kinesin-1 because the changes occur for low motor concentration for Kif4A (tens of picomolar) versus microtubule lattice changes induced by kinesin-1 (tens of nanomolar) (25, 26). Two-color experiments with Kif4A and kinesin-1 presented here show changes in the run length, lifetime, and velocity of Kif4A with increasing motor concentration, while motility of kinesin-1 did not appear to change significantly (Fig. 4). As a result, long-range motor coupling can drive end-tag formation for Kif4A but not kinesin-1. Our findings therefore suggest that long-range motor coupling can diversify the possible outcomes of collective motor activity on microtubules, depending on the properties of individual proteins (Fig. 7B).

Previous work has proposed that conformational changes in tubulin heterodimers mediated by the binding of microtubule-associated proteins can act as an allosteric coupler within the microtubule lattice (30, 31). Our findings broaden the scenario in which these effects are relevant by suggesting, as in previous work (25), that the molecular and structural alterations mediating microtubule allosteric coupling do not require a saturated microtubule lattice. Consistent with this, our model is able to explain the experimental results while assuming that any changes to the microtubule are rapidly reversible on the timescale of seconds. This, together with previous work (26, 27), suggests that long-distance coupling can be achieved without requiring long-term alteration of the microtubule lattice. In contrast, mechanisms such as tubulin isoform diversity, posttranslational modification, and protofilament register shifts are long lived or irreversible structural/biochemical changes to the microtubule. Transient motor-autonomous long-distance coupling might confer a unique advantage, as microtubules can quickly respond to changes in protein concentration to regulate kinesin motility.

The long-range coupling we describe has significant implications for motor-based cellular processes because only a small number of motors need to bind on a microtubule to trigger a cascade (25) (Movie S2). For example, in the context of intracellular transport, long-range coupling could facilitate changes in

velocity, motor force–velocity relation, or the outcome of tug-of-war between opposing motors, on a specific subset of cellular microtubules. Beyond coupling between motors, the long-range effects may also impact microtubule ends to control dynamic instability. For example, increased Kif4A processivity can increase the protein concentration at microtubule ends, which could then alter the polymerization of dynamic microtubules (23). Thus low-density, long-distance interactions may allow motors to self-organize without physical short-range coupling, oligomerization, binding partners, or tubulin posttranslational modifications. This kind of coupling can make kinesin motors more adaptable, allowing them to perform different functions depending on the surrounding environment and local motor concentration in cells.

Our results add to the growing body of work suggesting a different view in which the microtubule is not a passive highway on which motors move, but instead a responsive medium that couples motors moving along it. Motors moving along microtubules may therefore be analogous to other physical systems in which other forms of collective behavior occur due to coupling through a medium, such as Cooper-paired electrons in a superconductor (56), diffusion of atoms of the surface of a crystal (57), liquid–liquid phase separation in an elastic gel (58, 59), and interactions of active particles through a granular medium (60).

Materials and Methods

In vitro fluorescence microscopy experiments were performed as described previously (24). To visualize the accumulation of Kif4A on microtubules, rhodamine-labeled biotinylated microtubules were immobilized in a flow chamber coated with neutravidin (0.2 mg/mL). Next, Kif4A-GFP and 1 mM ATP were flushed into the flow chamber in assay buffer (BRB80 buffer supplemented with 1 mM tris(2-carboxyethyl)phosphine (TCEP), 0.2 mg/mL k-casein, 20 μ M taxol, 40 mg/mL glucose oxidase, 35 mg/mL glucose catalase, 0.5% β -mercaptoethanol, 5% sucrose, and 1 mM ATP). The flow cell was incubated for 10 min before imaging of the microtubule and motors. Single molecule experiments were performed similarly except a time-lapse sequence of images was immediately acquired at a rate of 0.3 frames per second after addition of Kif4A-GFP and ATP into the flow chamber. Experiments with unlabeled K401, Kif4A-mCherry, and K401-clip-647 were also performed using the same method. All experiments were performed on a Nikon Ti-E inverted microscope with a Ti-ND6-PFS perfect focus system equipped with an APO TIRF 100 \times oil/1.49 NA objective (Nikon).

Data Availability. Images, simulation code, and simulation results data have been deposited in GitHub (<https://github.com/Betterton-Lab/CyLaKS>) (61). All other data are included in this article and/or *SI Appendix*.

ACKNOWLEDGMENTS. We thank Matthew Glaser, Dick McIntosh, Michael Shelley, and Daniel Needleman for useful discussions. We thank Nandini Mani for help with protein purification and BLI assay. This work was funded by NSF Grant DMR-1725065 (to M.D.B.) and NIH Grants R01GM124371 (to M.D.B.) and 1DP2GM126894 (to R.S.). Simulations used the Summit supercomputer, supported by NSF Grants ACI-1532235 and ACI-1532236.

Author affiliations: ^aDepartment of Genetics, Harvard Medical School, Boston, MA 02115; ^bDepartment of Molecular Biology, Massachusetts General Hospital, Boston, MA 02114; ^cDepartment of Physics, University of Colorado Boulder, Boulder, CO 80309; ^dDepartment of Molecular, Cellular, and Developmental Biology, University of Colorado Boulder, Boulder, CO 80309; and ^eCenter for Computational Biology, Flatiron Institute, New York, NY 10010

1. H. E. Huxley, W. Brown, The low-angle x-ray diagram of vertebrate striated muscle and its behaviour during contraction and rigor. *J. Mol. Biol.* **30**, 383–434 (1967).
2. R. Craig, J. L. Woodhead, Structure and function of myosin filaments. *Curr. Opin. Struct. Biol.* **16**, 204–212 (2006).
3. I. R. Gibbons, A. J. Rowe, Dynein: A protein with adenosine triphosphatase activity from cilia. *Science* **149**, 424–426 (1965).

4. T. J. Mitchison, H. M. Mitchison, Cell biology: How cilia beat. *Nature* **463**, 308–309 (2010).
5. K. G. Kozminski, K. A. Johnson, P. Forscher, J. L. Rosenbaum, A motility in the eukaryotic flagellum unrelated to flagellar beating. *Proc. Natl. Acad. Sci. U.S.A.* **90**, 5519–5523 (1993).
6. B. Prevo, J. M. Scholey, E. J. G. Peterman, Intraflagellar transport: Mechanisms of motor action, cooperation, and cargo delivery. *FEBS J.* **284**, 2905–2931 (2017).

7. W. Saunders, V. Lengyel, M. A. Hoyt, Mitotic spindle function in *Saccharomyces cerevisiae* requires a balance between different types of kinesin-related motors. *Mol. Biol. Cell* **8**, 1025–1033 (1997).
8. E. N. Cytrynbaum, J. M. Scholey, A. Mogilner, A force balance model of early spindle pole separation in *Drosophila* embryos. *Biophys. J.* **84**, 757–769 (2003).
9. V. Syrovatkina, C. Fu, P. T. Tran, Antagonistic spindle motors and MAPs regulate metaphase spindle length and chromosome segregation. *Curr. Biol.* **23**, 2423–2429 (2013).
10. R. Blackwell *et al.*, Physical determinants of bipolar mitotic spindle assembly and stability in fission yeast. *Sci. Adv.* **3**, e1601603 (2017).
11. M. A. Welte, Bidirectional transport along microtubules. *Curr. Biol.* **14**, R525–R537 (2004).
12. M. J. I. Müller, S. Klumpp, R. Lipowsky, Tug-of-war as a cooperative mechanism for bidirectional cargo transport by molecular motors. *Proc. Natl. Acad. Sci. U.S.A.* **105**, 4609–4614 (2008).
13. N. D. Derr *et al.*, Tug-of-war in motor protein ensembles revealed with a programmable DNA origami scaffold. *Science* **338**, 662–665 (2012).
14. M. Linari *et al.*, Force generation by skeletal muscle is controlled by mechanosensing in myosin filaments. *Nature* **528**, 276–279 (2015).
15. C. Leduc *et al.*, Molecular crowding creates traffic jams of kinesin motors on microtubules. *Proc. Natl. Acad. Sci. U.S.A.* **109**, 6100–6105 (2012).
16. D. M. Miedema *et al.*, Correlation imaging reveals specific crowding dynamics of kinesin motor proteins. *Phys. Rev. X* **7**, 041037 (2017).
17. A. Vilfan *et al.*, Dynamics and cooperativity of microtubule decoration by the motor protein kinesin. *J. Mol. Biol.* **312**, 1011–1026 (2001).
18. W. H. Roos *et al.*, Dynamic kinesin-1 clustering on microtubules due to mutually attractive interactions. *Phys. Biol.* **5**, 046004 (2008).
19. M. L. Gupta Jr., P. Carvalho, D. M. Roof, D. Pellman, Plus end-specific depolymerase activity of Kip3, a kinesin-8 protein, explains its role in positioning the yeast mitotic spindle. *Nat. Cell Biol.* **8**, 913–923 (2006).
20. V. Varga *et al.*, Yeast kinesin-8 depolymerizes microtubules in a length-dependent manner. *Nat. Cell Biol.* **8**, 957–962 (2006).
21. V. Varga, C. Leduc, V. Bormuth, S. Diez, J. Howard, Kinesin-8 motors act cooperatively to mediate length-dependent microtubule depolymerization. *Cell* **138**, 1174–1183 (2009).
22. C. Zhu, W. Jiang, Cell cycle-dependent translocation of PRC1 on the spindle by Kif4 is essential for midzone formation and cytokinesis. *Proc. Natl. Acad. Sci. U.S.A.* **102**, 343–348 (2005).
23. P. Bieling, I. Kronja, T. Surrey, Microtubule motility on reconstituted meiotic chromatin. *Curr. Biol.* **20**, 763–769 (2010).
24. R. Subramanian, S. C. Ti, L. Tan, S. A. Darst, T. M. Kapoor, Marking and measuring single microtubules by PRC1 and kinesin-4. *Cell* **154**, 377–390 (2013).
25. E. Muto, H. Sakai, K. Kaseda, Long-range cooperative binding of kinesin to a microtubule in the presence of ATP. *J. Cell Biol.* **168**, 691–696 (2005).
26. T. Shima *et al.*, Kinesin-binding-triggered conformation switching of microtubules contributes to polarized transport. *J. Cell Biol.* **217**, 4164–4183 (2018).
27. D. R. Peet, N. J. Burroughs, R. A. Cross, Kinesin expands and stabilizes the GDP-microtubule lattice. *Nat. Nanotechnol.* **13**, 386–391 (2018).
28. K. Sekimoto, J. Prost, Elastic anisotropy scenario for cooperative binding of kinesin-coated beads on microtubules. *J. Phys. Chem. B* **120**, 5953–5959 (2016).
29. S. Triclin *et al.*, Self-repair protects microtubules from their destruction by molecular motors. *Nat. Mater.* **20**, 883–891 (2021).
30. M. Zanic, P. O. Widlund, A. A. Hyman, J. Howard, Synergy between XMAP215 and EB1 increases microtubule growth rates to physiological levels. *Nat. Cell Biol.* **15**, 688–693 (2013).
31. T. Kim, L. M. Rice, Long-range, through-lattice coupling improves predictions of microtubule catastrophe. *Mol. Biol. Cell* **30**, 1451–1462 (2019).
32. S. A. Fiorenza, D. G. Steckhahn, M. D. Betterton, Modeling spatiotemporally varying protein-protein interactions in CyLaKS, the Cytoskeleton Lattice-based Kinetic Simulator. *Eur. Phys. J. E* **44**, 105 (2021).
33. S. Wijeratne, R. Subramanian, Geometry of antiparallel microtubule bundles regulates relative sliding and stalling by PRC1 and Kif4A. *eLife* **7**, e32595 (2018).
34. A. Parmeggiani, T. Franosch, E. Frey, Totally asymmetric simple exclusion process with Langmuir kinetics. *Phys. Rev. E Stat. Nonlin. Soft Matter Phys.* **70**, 046101 (2004).
35. L. E. Hough, A. Schwabe, M. A. Glaser, J. R. McIntosh, M. D. Betterton, Microtubule depolymerization by the Kinesin-8 motor Kip3p: A mathematical model. *Biophys. J.* **96**, 3050–3064 (2009).
36. L. Reese, A. Melbinger, E. Frey, Crowding of molecular motors determines microtubule depolymerization. *Biophys. J.* **101**, 2190–2200 (2011).
37. H. S. Kuan, M. D. Betterton, Biophysics of filament length regulation by molecular motors. *Phys. Biol.* **10**, 036004 (2013).
38. L. Reese, A. Melbinger, E. Frey, Molecular mechanisms for microtubule length regulation by kinesin-8 and XMAP215 proteins. *Interface Focus* **4**, 20140031 (2014).
39. H. S. Kuan, M. D. Betterton, Motor protein accumulation on antiparallel microtubule overlaps. *Biophys. J.* **110**, 2034–2043 (2016).
40. H. S. Kuan, M. D. Betterton, Phase-plane analysis of the totally asymmetric simple exclusion process with binding kinetics and switching between antiparallel lanes. *Phys. Rev. E* **94**, 022419 (2016).
41. T. Duke, S. Leibler, Motor protein mechanics: A stochastic model with minimal mechanochemical coupling. *Biophys. J.* **71**, 1235–1247 (1996).
42. A. B. Kolomeisky, E. B. Stukalin, A. A. Popov, Understanding mechanochemical coupling in kinesins using first-passage-time processes. *Phys. Rev. E Stat. Nonlin. Soft Matter Phys.* **71**, 031902 (2005).
43. S. Liepelt, R. Lipowsky, Kinesin's network of chemomechanical motor cycles. *Phys. Rev. Lett.* **98**, 258102 (2007).
44. D. Chowdhury, Modeling stochastic kinetics of molecular machines at multiple levels: From molecules to modules. *Biophys. J.* **104**, 2331–2341 (2013).
45. J. A. Wagoner, K. A. Dill, Molecular motors: Power strokes outperform Brownian ratchets. *J. Phys. Chem. B* **120**, 6327–6336 (2016).
46. A. Šarlah, A. Vilfan, Minimum requirements for motility of a processive motor protein. *PLoS One* **12**, e0185948 (2017).
47. R. Takaki, M. L. Mugnai, Y. Goldtzyk, D. Thirumalai, How kinesin waits for ATP affects the nucleotide and load dependence of the stepping kinetics. *Proc. Natl. Acad. Sci. U.S.A.* **116**, 23091–23099 (2019).
48. D. D. Hackney, Kinesin ATPase: Rate-limiting ADP release. *Proc. Natl. Acad. Sci. U.S.A.* **85**, 6314–6318 (1988).
49. W. Hua, E. C. Young, M. L. Fleming, J. Gelles, Coupling of kinesin steps to ATP hydrolysis. *Nature* **388**, 390–393 (1997).
50. R. A. Cross, The kinetic mechanism of kinesin. *Trends Biochem. Sci.* **29**, 301–309 (2004).
51. A. B. Asenjo, Y. Weinberg, H. Sosa, Nucleotide binding and hydrolysis induces a disorder-order transition in the kinesin neck-linker region. *Nat. Struct. Mol. Biol.* **13**, 648–654 (2006).
52. J. O. Andreasson *et al.*, Examining kinesin processivity within a general gating framework. *eLife* **4**, e07403 (2015).
53. K. J. Mickolajczyk *et al.*, Kinetics of nucleotide-dependent structural transitions in the kinesin-1 hydrolysis cycle. *Proc. Natl. Acad. Sci. U.S.A.* **112**, E7186–E7193 (2015).
54. K. J. Mickolajczyk, W. O. Hancock, Kinesin processivity is determined by a kinetic race from a vulnerable one-head-bound state. *Biophys. J.* **112**, 2615–2623 (2017).
55. W. O. Hancock, The kinesin-1 chemomechanical cycle: Stepping toward a consensus. *Biophys. J.* **110**, 1216–1225 (2016).
56. B. Keimer, S. A. Kivelson, M. R. Norman, S. Uchida, J. Zaanen, From quantum matter to high-temperature superconductivity in copper oxides. *Nature* **518**, 179–186 (2015).
57. M. Ø. Pedersen *et al.*, Diffusion of N adatoms on the Fe(100) surface. *Phys. Rev. Lett.* **84**, 4898–4901 (2000).
58. R. W. Style *et al.*, Liquid-liquid phase separation in an elastic network. *Phys. Rev. X* **8**, 011028 (2018).
59. K. A. Rosowski *et al.*, Elastic ripening and inhibition of liquid-liquid phase separation. *Nat. Phys.* **16**, 422–425 (2020).
60. N. Kumar, H. Soni, S. Ramaswamy, A. K. Sood, Flocking at a distance in active granular matter. *Nat. Commun.* **5**, 4688 (2014).
61. S. A. Fiorenza, *et al.*, The Cytoskeleton Lattice-based Kinetic Simulator (CyLaKS). GitHub. <https://github.com/Betterton-Lab/CyLaKS>. Deposited 19 March 2021.